16th Australasian Fluid Mechanics Conference
Crown Plaza, Gold Coast, Australia
2-7 December 2007

Unsteady flow around a Rectangular Cylinder

C. W. Pun and P. L. O'Neill

School of Mechanical Engineering
University of Western Australia, Western Australia, 6009 AUSTRALIA

Abstract

This paper describes an investigation into the unsteady flow behaviour around a rectangular cylinder using particle image velocimetry (PIV). Instantaneous and average velocity fields were obtained from PIV images. Analysis of the structures observed in the instantaneous velocity fields reveals the presence of small scale (Kelvin-Helmholtz) vortex structures in the shear layer that separates at the leading edge of the rectangular cylinder, and evidence of von Karman vortex shedding was observed in the wake region.

Introduction

The flow structure and wake formation around a bluff body in a uniform flow has been investigated by many researchers during the past century or more. Interest in this topic is motivated by the desire to understand the fundamental characteristics of bluff body aerodynamics as well as its direct relevance in engineering applications. According to Okajima (1982) [6], for flow around rectangular cylinders at very low Reynolds numbers separation occurs at the trailing edge, while at the leading edge there is immediate reattachment following separation. As the Reynolds number increases, separation at the leading edge develops and, depending on the ratio of cylinder width to height and the Reynolds number, reattachment may or may not occur. Okajima (1982) [6] describes two modes for flow around a rectangular cylinder. In Mode I the flow separates from the leading edge and reattaches on the side surfaces of the rectangular cylinder. Such a flow will lead to a narrow wake flow. In Mode II reattachment is not possible and a wider wake flow results. For a width to height ratio of 2, Okajima found that the transition from Mode I to Mode II occurred at a Reynolds number around 500 based on the free stream velocity and the height of the rectangular cylinder, but at higher width to height ratios, the transition occurred either at higher Reynolds numbers or did not occur at all, as the separated flow always reattached to the side surfaces of the cylinder.

Some of the work on bluff body flows has used flow visualisations, which need to be interpreted with care, as they may not represent the true flow behaviour. For example Hama (1962) [4] reported that the rolling up of a streakline may not necessarily constitute a positive identification of a discrete vortex. Furthermore, differences in the diffusivity of the vorticity in comparison to the diffusivity of the flow tracer will lead to misrepresentations of vortices. Smits and Lim (2000) [9] noted that at low Reynolds numbers (less than 100) vorticity diffuses more rapidly than the flow tracer, whereas in turbulent flows the tracers will diffuse more rapidly than the vorticity. The streaklines will also vary depending on the location at which they are introduced. Cimbala et al. (1988) [1] attributed this to a memory effect. Given the problems associated with interpretation of flow visualisations, it is desirable to confirm the understandings developed from flow visualisations using some other technique.

In this study, particle image velocimetry (PIV) is used to observe the characteristics of the flow structure that develops around a rectangular cylinder in a uniform flow. Instantaneous and time averaged representations of the velocity field are used to analyse the spatial structures present in the separated shear layer and wake. Although testing was conducted over a range of Reynolds numbers from 8,100 to 35,400, in this paper only results from two Reynolds numbers (10,000 and 20,000) are presented. The Reynolds number is based on the height of the rectangular cylinder, which is 30 mm, and the average streamwise velocity determined at the same position as the rectangular cylinder, but without the rectangular cylinder in place. This velocity is equivalent to the average free stream velocity.

Experimental method

The particle image velocimetry studies were conducted in an open circuit boundary layer wind tunnel equipped with a centrifugal fan, wide angle diffuser, settling chamber comprising one screen, followed by a honeycomb, followed by two more screens, a 9:1 contraction and a working section. The working section is 250 mm high, 380 mm wide and 1850 mm in length. The roof and floor of the wind tunnel working section are made of medium density fibreboard, but the roof has an acrylic glass window running along its centre to allow for optical access. The walls of the working section are made of acrylic glass, which allows a clear view of the working section from either side.

Background turbulence intensity in the wind tunnel was determined using PIV in a region approximately 350 mm downstream from the contraction. This region was chosen as it had previously been reported that the lowest turbulence intensity for the working section occurred in that region (Soria, 1988) [10], and it was planned that the rectangular cylinder experiments would be run in that location. The imaged region measured 119 mm in the downstream direction and 88 mm in the cross stream direction. The turbulence intensity was measured over a range of velocities from 5 m/s to 15 m/s. At 5 m/s turbulence intensity was around 2%, but that dropped to 1% at 10 m/s before increasing again to around 2% at 15m/s. It is noted, however, that other techniques would give a more accurate assessment of turbulence intensity, and PIV probably overestimates the true value.

The rectangular cylinder used in this study was manufactured from solid steel. It measured 60 mm in the streamwise direction and 30 mm in the cross stream direction, and was wide enough to fit snugly between the walls of the wind tunnel. It was located 340 mm downstream from the contraction and 140 mm above the floor and was rigidly mounted on plates attached to the floor of the wind tunnel. The model had a smooth surface and was painted black to minimise reflection during PIV acquisition. Configuration of the rectangular cylinder, laser and camera during PIV acquisition is shown in Figure 1.

Two areas were chosen for PIV imaging, and these are shown in Figure 2. The bottom edge of the images acquired of region A was 1.5 mm above the upper surface of the rectangular cylinder. The images acquired at this position covered an area measuring

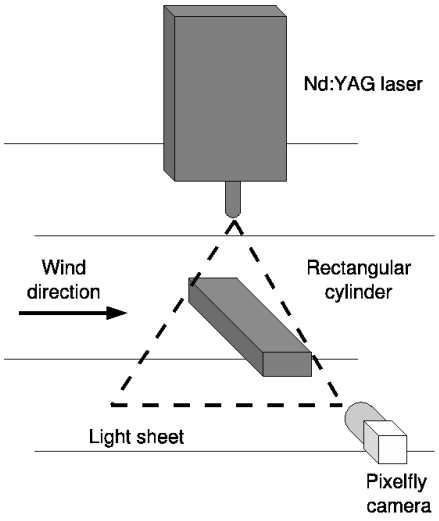

Figure 1: Experimental set up. The Nd:YAG laser is located above the working section of the wind tunnel, the camera faces the laser light sheet.

66 mm in the streamwise direction and 48 mm in the cross stream direction and captured the separated shear layer from the leading edge of the rectangular cylinder. The front edge of the images acquired of region B was 1 mm downstream from the rectangular cylinder, and the images acquired covered an area measuring 133 mm in the streamwise direction and 77 mm in the cross stream direction. Images acquired at this position captured the wake flow behind the rectangular cylinder.

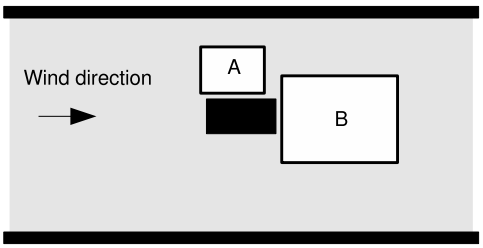

Figure 2: Imaging regions for PIV experiments. Region A included the separated shear layer, while region B covered the wake flow.

The particles used for PIV imaging were generated by a Laskin nozzle droplet generator with olive oil as the droplet constituent. Particles were introduced to the wind tunnel by placing the outlet from the droplet generator inside the filter box at the wind tunnel inlet. Laser light to illuminate the particles was provided by a New Wave Solo 15 Nd:YAG PIV laser, which has two laser cavities for the two laser pulses required to acquire dual images for PIV analysis. The scattered light from the seed particles was recorded by a PCO Pixelfly camera, which has a CCD array of size 1390 pixels by 1024 pixels and 12 bit resolution and was fitted with a 50 mm Nikon lens with f-stop set at 8. The reproduction ratio at for region A gave a spatial resolution of 47 micrometres/pixel, while the spatial resolution for region B was more than double that at 96 micrometres/pixel. Timing of the laser and camera was controlled via PIVSync software from ILA (Germany) installed on a computer running under a Windows operating system.

The particle image pairs acquired for correlation were analysed using the MCCDPIV (multi-grid cross correlation digital PIV) software described in Soria et al. (1999) [13]. The MCCDPIV algorithm involves:

1. Cross correlation of matching interrogation windows in two single-exposed images. This step determines a first estimate of the displacement field. The quality and consistency of the displacement estimates in the first cross correlation is assessed using a number of techniques, including the method of Hart (2000) [5].
2. The interrogation window in the second single exposed image is then offset by a distance equivalent to the local displacement vector estimated in step 1. Cross correlation is then performed using the original interrogation window in the first single exposed image and the offset interrogation window in the second single exposed image. Once the displacements are determined for all of the interrogation windows, the quality and consistency of the displacement estimates are checked, again using a number of techniques, but not the method of Hart (2000) [5].

For the images taken of the initial formation of the shear layer directly above the beam, the spacing between vectors was 8 pixels in both the horizontal and vertical directions. In the first correlation, a square interrogation window of size 32 pixels was used, resulting in 75% overlap between adjacent interrogation windows. In the second correlation a square interrogation window of size 16 pixels was used.

The quality and consistency of the displacements was checked using the following methods:

1. a maximum velocity ratio check (displacements larger than some fraction of the first interrogation window were identified as erroneous displacements)
2. a global histogram check [8];
3. a median displacement check [14];
4. and a dynamic mean displacement check [8].

These tests were applied in order as listed.

For the images taken in the wake of the beam, the spacing between vectors was 16 pixels in both the horizontal and vertical directions. In the first cross correlation a square interrogation window of size 64 pixels was used, while in the second cross correlation a square interrogation window of size 32 pixels was used. In addition to the checks on the quality and consistency of the displacements used in the leading shear layer, a check on the cross correlation coefficient was used. This check was applied before the four checks listed above.

The out of plane vorticity was calculated from the velocity measurements according to the technique described in Soria (1996a) [11], whereby the local velocity gradients are obtained from a 13 point, two dimensional fit to the local velocity data.

In order to compare the velocity and vorticity results at different Reynolds numbers, the results were nondimensionalised. In the case of velocity, non-dimensionalisation involved dividing the results by the free stream velocity. In the case of vorticity, non-dimensionalisation involved dividing by the ratio of the free stream velocity to the height of the beam.

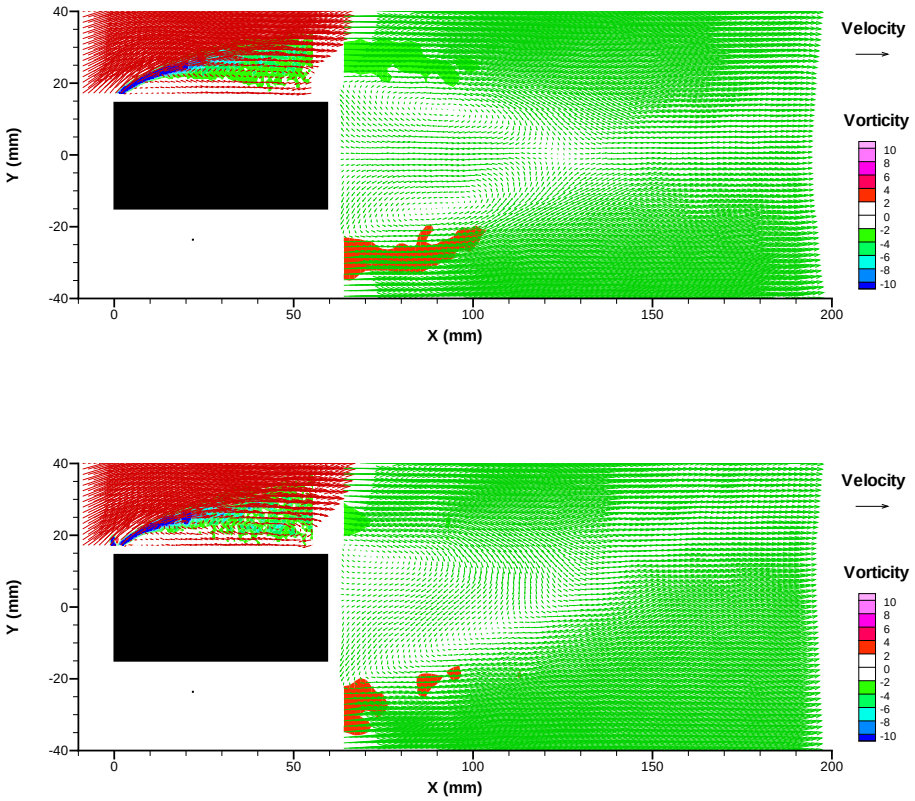

Figure 3: Average velocity field for Re=10,000 (top) and Re=20,000 (bottom). The rectangular cylinder cross section is shown in black. Note that only every fourth vector is plotted in the region above the rectangular cylinder. Velocity and vorticity are non-dimensionalised as described in the text. The reference vector indicates the velocity across the central section of the wind tunnel with no obstructions in the flow.

Results

The two Reynolds numbers chosen for comparison were 10,000 and 20,000. These were chosen because they were the minimum and maximum Reynolds number for which PIV images could be acquired of both the separated shear layer and the wake. Due to the speed of the flow, it was not possible to obtain images of the separated shear layer over the entire range of flow rates possible in the wind tunnel. This was because the time separation between consecutive images in an image pair needed for PIV was shorter than the minimum time that the PIV equipment could achieve. One hundred image pairs were recorded for analysis at both these Reynolds numbers for both regions A and B.

Average Velocity and Vorticity

The average velocity fields at the two specified Reynolds numbers were determined, and these are plotted in Figure 3. From these plots it is easy to see the separated shear layer above the rectangular cylinder and the wake behind the rectangular cylinder. The vectors are much more closely spaced in the region above the rectangular cylinder than they are in the wake region. In fact, only every fourth average vector determined is plotted in the region above the rectangular cylinder, while every average vector determined is plotted behind the cylinder. The higher magnification is one of the factors that contributes to this increased vector density, but the quality of the images allowed us to conduct the PIV analysis at a smaller grid spacing. The closer vector spacing is also reflected in the vorticity contours where the closely spaced vectors are reflected in an irregular vorticity contour in comparison to the smooth contours seen in the wake region.

Some differences can be seen between the flow fields at the different Reynolds numbers. At the higher Reynolds number there appears to be a region of concentrated vorticity just ahead of the separation that does not occur at the lower Reynolds number, but apart from this the flow in this region is very similar at the two Reynolds numbers. A feature of this region in both cases is a large (average) recirculation region between the separated shear layer and the top of the rectangular cylinder.

In the wake region the flow is quite different in the two cases. For the lower Reynolds number case the wake flow is symmetric with two recirculation bubbles downstream from the trailing edge of the rectangular cylinder. At the higher Reynolds number the wake flow is not symmetric and it appears that, on average, the upper shear layer is pulled across the wake before the lower shear layer is pulled across the wake. A number of reasons for this result were considered. Buoyancy was firstly considered, although experimental data taken before and after this result at different Reynolds numbers show symmetric wake flows, and it is unlikely that buoyancy only influenced the result at this Reynolds number. Another possibility takes into account the periodic nature of the wake flow. If the timing of

image acquisition was such that it was biased towards acquiring images for a particular form of the wake flow, this could result in an asymmetric average wake flow. Investigating this further, Figure 4 presents contours for the largest values of standard deviation from the mean velocity in the streamwise direction, normalised by the free stream velocity, for the two cases of Re=10,000 and Re=20,000. The plot for Re=10,000 is quite symmetric, while that for Re=20,000 is quite unsymmetric. The highest standard deviations, or rms, values occur in those regions around the separated shear layer. The larger standard deviation in the upper separated shear layer at Re=20,000 could be due to a greater amount of variation in the position of the separated shear layer across all the images analysed, in comparison to the relatively small variation in the position of the lower separated shear layer.

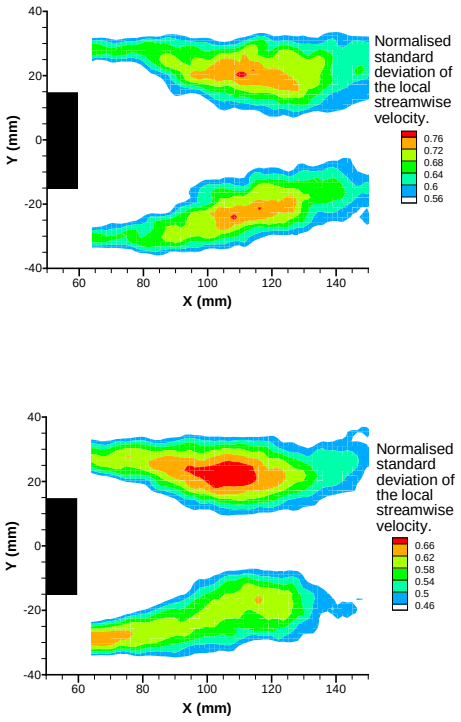

Figure 4: Normalised standard deviation for the streamwise component of velocity for Re=10,000 (top) and Re=20,000 (bottom).

Another factor to be considered is the number of samples used to determine the mean velocity. Soria (1996b) [12] reported that the type of PIV algorithm used in this study gives a confidence interval on the local displacement of the order of $\pm$ 0.1 pixels at the 95% confidence level. The confidence interval on the mean displacement cannot be better than the confidence interval on the individual data points, so using a binomial distribution, as described in Grant et al. (1992) [3], the number of samples required for the calculation of the mean displacement to this level of confidence was determined, and is shown in Figure 5 for the two Reynolds numbers investigated. In some areas of the flow field more than 3000 samples would be required to achieve this confidence interval. These regions correspond to areas in the flow with high turbulence intensity, which is consistent with the findings of Grant et al. (1992) [3]. With the 100 displacement fields available, the maximum confidence interval on the local mean displacement was found to be $\pm$ 0.7 pixels at the 95% confidence level. Given the large confidence interval on the calculation of the mean displacement, the remainder of this paper is devoted to instantaneous velocity and vorticity data. Information on parameters that require an accurate determination of the mean flow field, such as the fluctuating velocity components, are not included in this paper.

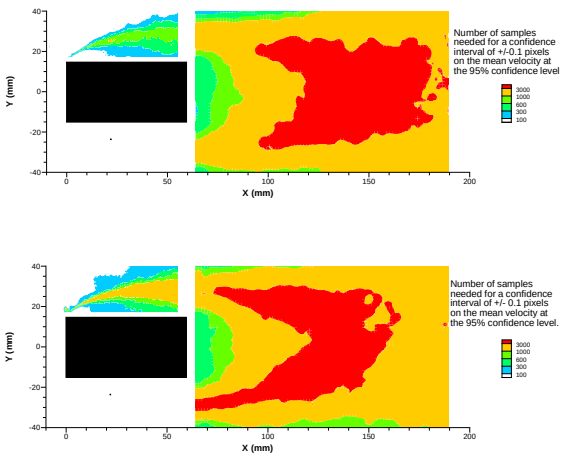

Figure 5: Number of samples required for a $\pm$ 0.1 pixel confidence interval on the mean at the 95% confidence level. Re=10,000 (top) and Re=20,000 (bottom).

Instantaneous Velocity and Vorticity

Due to the unsteady nature of the flow studied, there is a lot of variation amongst the velocity fields obtained at each of the Reynolds numbers. This is shown in Figure 6, which shows some examples of the instantaneous velocity and vorticity field in the region above the rectangular cylinder for the lower Reynolds number case. Unlike the average velocity field for this region shown in Figure 3, every vector is plotted. These velocity fields were chosen as they show quite different positions of the separated shear layer. In the top image the region of retarded flow below the separated shear layer extends no further than approximately 30 mm in the y direction (i.e. 15 mm above the surface of the rectangular cylinder). In the middle image the retarded flow region extends not further than 20 mm above the top surface of the rectangular cylinder. In the bottom image, the retarded flow region extends not further than 25 mm above the top surface of the rectangular cylinder.

In all the plots in Figure 6, small scale coherent vortical structures in the separated shear layer are present. These are Kelvin-Helmholtz vortices associated with the Kelvin-Helmholtz instabilities due to the strong velocity gradient in the separated shear layer. A small perturbation in the vortex sheet that is seen to extend from the leading edge of the rectangular cylinder causes the sheet to roll up into a vortex. Generally the formation of Kelvin-Helmholtz vortices is described as a periodic array of vortices, but in this case, the coherent vortices seen near the start of the separated shear layer appear to be entrained into the recirculation region below the separated shear layer, before becoming mostly incoherent, so the periodicity associated with the formation of Kelvin-Helmholtz vortices is not clearly evident in these instantaneous images. This is further illustrated by the streamline and vorticity plot shown in Figure 7. This is plotted from the velocity field that was shown at the top of Figure 6. From the streamline plot the entrainment of the vortices formed in the separated shear layer is apparent,

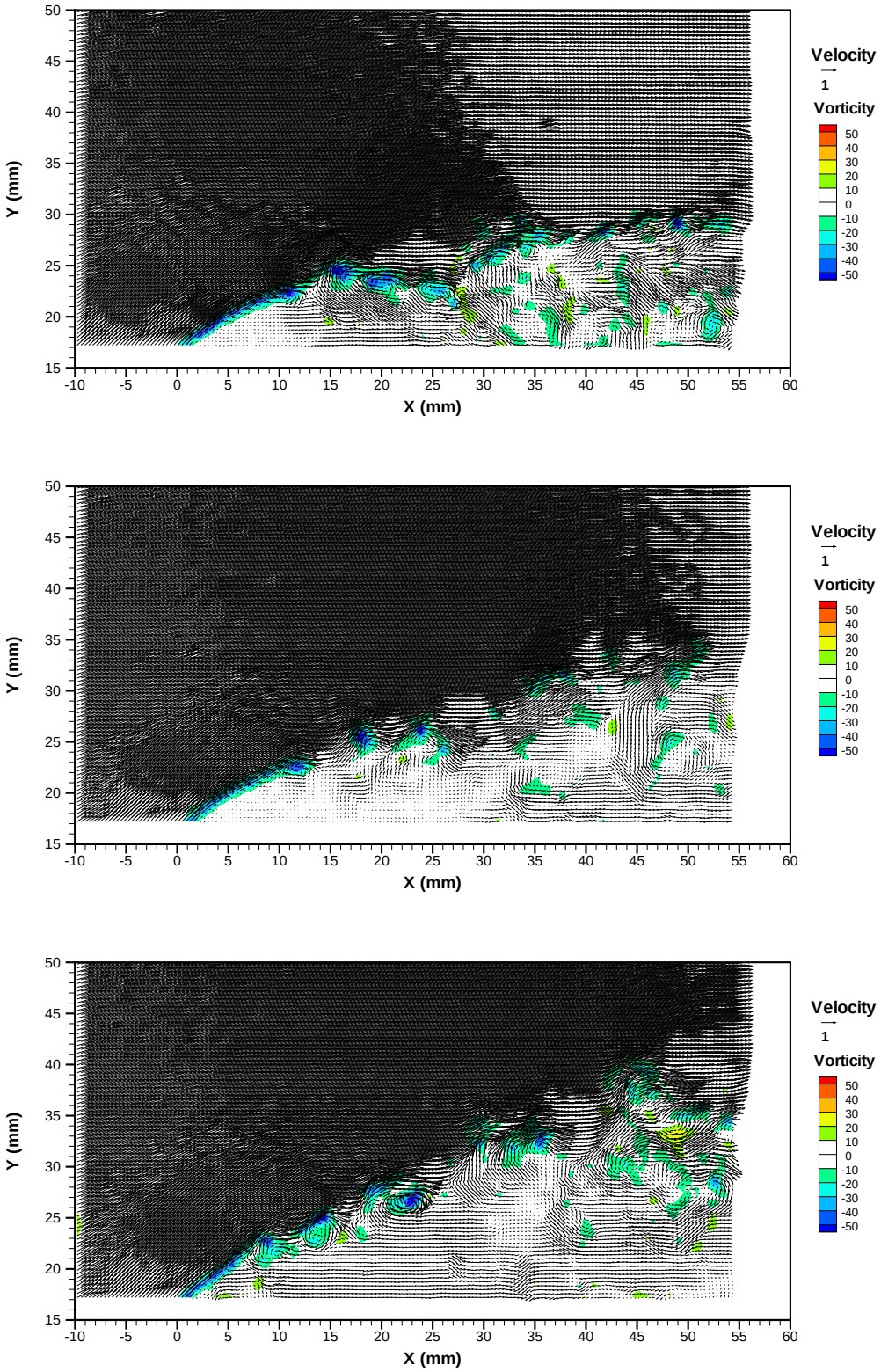

Figure 6: Selected instantaneous velocity fields for Re=10,000. In this case every vector is plotted. The plots were chosen as they represent different stages in the development of the separated shear layer.

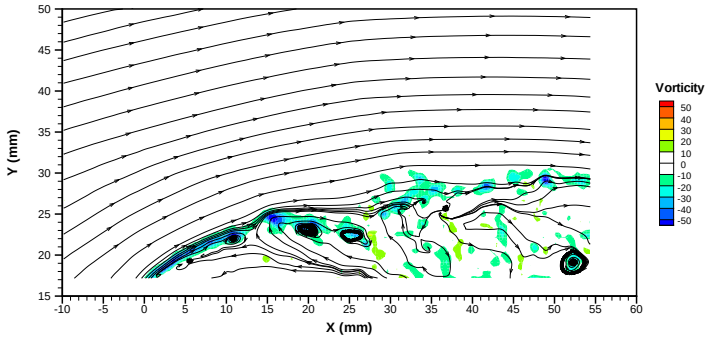

Figure 7: Example of instantaneous streamlines and vorticity for Re=10,000.

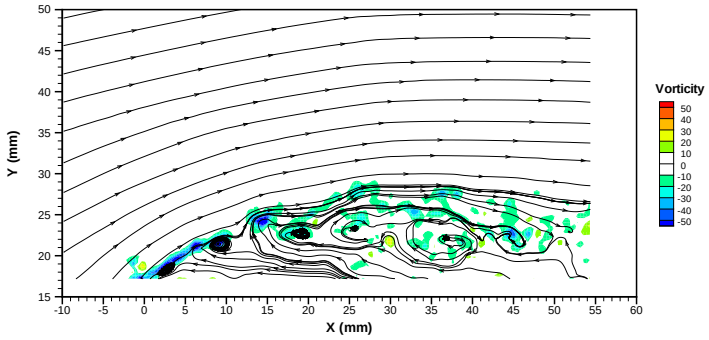

Figure 8: Example of instantaneous streamlines and vorticity for Re=20,000.

but also towards the trailing edge of the rectangular cylinder another vortex can be seen. As the vorticity has predominantly dissipated from the initial formation of the Kelvin-Helmholtz vortices, this coherent structure is believed to be the result of the interaction between the recirculation that occurs in the region between the separated shear layer and the top of the rectangular cylinder and the vortex shedding from the trailing edge of the rectangular cylinder. This downstream vortex was not present in all the instantaneous velocity fields obtained.

Instantaneous velocity fields at the higher Reynolds also exhibit the formation of Kelvin-Helmholtz vortices, however they appear to persist and even grow as they move downstream. This is illustrated by the streamline and vortex plot shown in Figure 9. This streamline plot does not show a vortex near the trailing edge of the rectangular cylinder, but it is present in other streamline plots in the series. Considering Figures 6 and 7, it appears that at the lower Reynolds number the first Kelvin-Helmholtz vortex is generated approximately 9-10 mm downstream from the leading edge of the rectangular cylinder (none of the other vector fields in the series showed K-H vortices closer to the leading edge). However, at the higher Reynolds number the first Kelvin-Helmholtz vortex is seen only 3 mm from the leading edge. The persistence and growth of the Kelvin-Helmholtz vortices and the earlier initiation of the Kelvin-Helmholtz vortices is consistent with the higher Reynolds number of the flow.

When considering the wake flow, again the unsteady nature of the flow under investigation produces a vast array of velocity fields. Two examples taken from the lower Reynolds number case are shown in Figure 9. The top image shows a large coherent vortex, probably shed from the upper surface trailing edge of the rectangular cylinder (i.e. it is a von Karman vortex). Slightly upstream from that coherent structure is a second oppositely signed von Karman vortex, probably shed from the bottom surface of the rectangular cylinder. Just downstream from these two opposing vortices the upper shear layer cuts across the wake, but further downstream again the lower surface layer crosses the wake. In the bottom image of Figure 9, a large positively signed vortex lies between streamlines that cross the wake from top to bottom, then from bottom to top. It is noted that this is an unusual position for a coherent vortex in the series of velocity fields - generally the coherent structure does not persist this far downstream from the trailing edge of the rectangular cylinder at this Reynolds number, presumably because the action of the shear layer cutting across the wake tends to break up the coherent vortex structures.

An example of the instantaneous streamlines and vorticity in the wake flow at the higher Reynolds number of 20,000 is shown in Figure 10. This shows a large vortex at a position approximately 95 mm downstream from the trailing edge of the rectangular cylinder. Note that this is an unusual image in the series of 100 taken at this Reynolds number. In all the other images there is no coherent vortex structure so far downstream, although there are many images with coherent vortex structures slightly upstream, around 65 mm downstream from the rectangular cylinder, the same position where the unusual coherent vortex structure was seen at the lower Reynolds number. As with the persistence and growth of the Kelvin-Helmholtz structures in the region above the rectangular cylinder, the evidence of vortical structures further downstream is consistent with the higher Reynolds number of the flow.

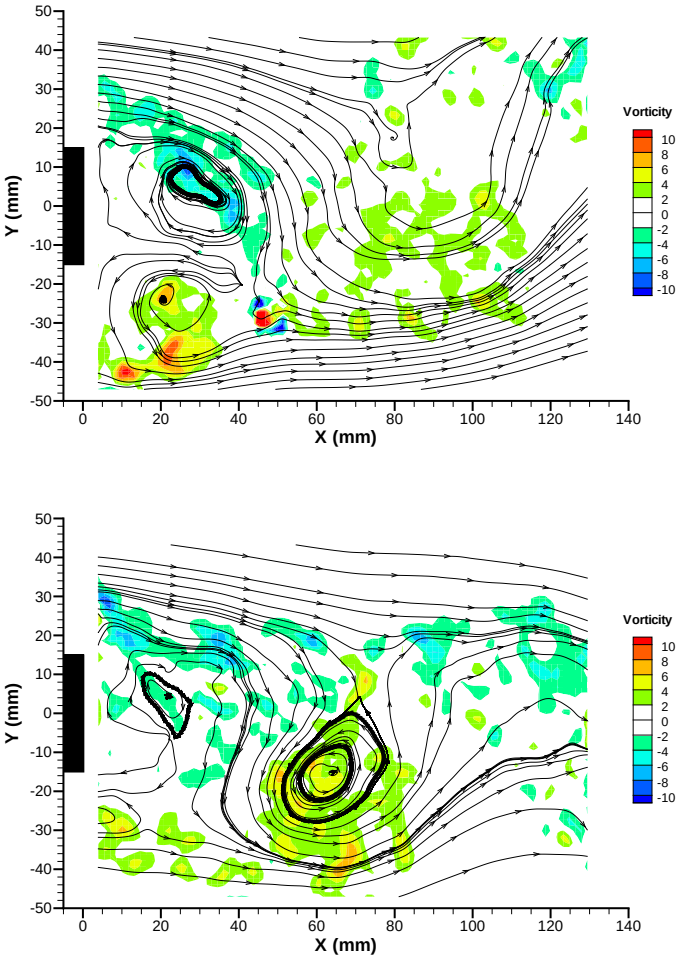

Figure 9: Examples of instantaneous streamlines and vorticity in the wake flow for Re=10,000.

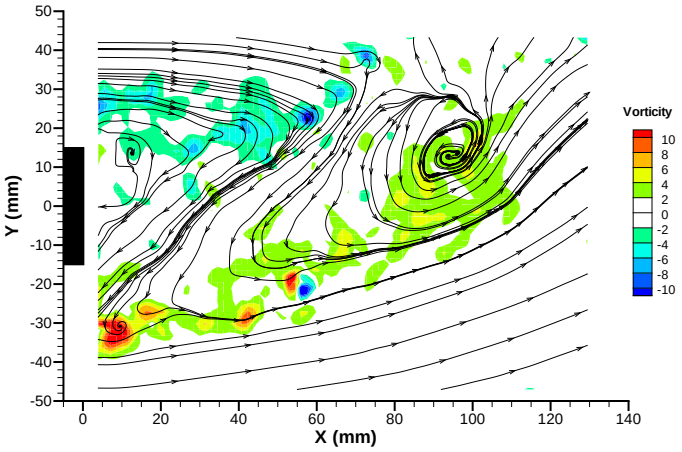

Figure 10: An example of instantaneous streamlines and vorticity in the wake flow for Re=20,000.

Discussion and Conclusions

The preceding plots of instantaneous flow in the separated shear layer and wake of a rectangular cylinder obtained using PIV reveal a rich and complex flow structure. Using the critical point descriptions of Perry and Chong (1987) [7], and keeping in mind that these are two dimensional representations in a non-moving reference frame, we can identify examples of stable focal points (eg. Figure 9, bottom image, (60,-15)), unstable focal points (eg. Figure 9, top image, (20,-25)), stable nodes (eg. Figure 8, (43,22)), unstable nodes (eg. Figure 9, top image, (40,-20)) and saddle points (eg. Figure 9, bottom image (15,-25)). Also in the wake plots are examples of both reverse flow and entrainment, as described in Gerrard (1966) [2], with the upper shear layer being entrained into the wake in, for example, the top image of Figure 9, and strong reverse flow in the region immediately downstream from the rectangular cylinder seen in Figure 10 where the direction of flow in the wake has a clear upstream component. In addition to these features there are Kelvin Helmholtz vortices in the shear layer separating from the leading edge of the rectangular cylinder, and von Karman vortices generated from the trailing edge of the rectangular cylinder.

It has previously been reported that the aerodynamic characteristics of flow around rectangular cylinders is relatively insensitive to Reynolds number, however the results presented here show some minor differences between the flow structure at the two Reynolds numbers of 10,000 and 20,000. The first difference was seen in the average velocity and vorticity plot for the region directly above the rectangular cylinder, where a region of concentrated vorticity was seen just ahead of the leading edge of the rectangular cylinder at Re=20,000 that was not seen at the lower Reynolds number. This would appear to be due to a transfer of momentum from the impact of the fluid on the bluff body to the fluid.

In the instantaneous velocity, vorticity and streamline plots, some other differences between the flow at the two Reynolds were observed. The Kelvin-Helmholtz vortices in the separating shear layer occurred closer to the leading edge of the rectangular cylinder at the higher Reynolds number than at the lower Reynolds number, and they appeared to grow in size as they moved downstream.This was in contrast to the lower Reynolds number case where these vortices appeared to be entrained into the recirculating flow between the top of the rectangular cylinder and the separated shear layer, where they appeared to substantially diffuse. Both the earlier initiation of the Kelvin-Helmholtz vortices and their persistence are consistent with a Reynolds number effect. The generation of a vortex near the trailing edge of the rectangular cylinder at both Reynolds numbers in some of the PIV data fields is attributed to an interaction between the formation of the von Karman vortex at the trailing edge of the rectangular cylinder and the recirculating flow along the surface of the rectangular cylinder.

In the case of the wake flow, the von Karman vortices shed from the trailing edge of the rectangular cylinder were also more persistent at the higher Reynolds number, and the flapping of the shear layer across the wake appeared to be substantially responsible for the diffusion of coherent vortex structures. The persistence of the von Karman vortices at higher Reynolds number is also consistent with a Reynolds number effect.

In this study, PIV has been applied to the flow around the rectangular cylinder at a resolution that has enabled us to demonstrate some of the topological features of this important flow. Further work using the data generated in this study will be aimed at examining the periodicity of the flow around a rectantular cylinder.

References

[1] Cimbala, J.M., Nagib, H.M. and Roshko, A. Large structure in the far wakes of two-dimensional bluff bodies, *Journal of Fluid Mechanics*, **190**, 1988, 256–298.

[2] Gerrard, J.H. The mechanics of the formation region of vortices behind bluff bodies, *Journal of Fluid Mechanics*, **25**, 1966, 401–413.

[3] Grant, I., Owens, E., Yan, Y.-Y. and Shen, X. Particle image velocimetry measurements of the separated flow behind a rearward facing step, *Experiments in Fluids*, **12**, 1992, 238–244.

[4] Hama, F.R. Streaklines in a perturbed shear flow, *Physics of Fluids*, **5**(6), 1962, 644–650.

[5] Hart, D.P. PIV error correction, *Experiments in Fluids*, **29**, 2000, 13–22.

[6] Okajima, A. Strouhal numbers of rectangular cylinders, *Journal of Fluid Mechanics*, **123**, 1982, 379–398.

[7] Perry, A.E. and Chong, M.S. A description of eddying motions and flow patterns using critical-point concepts, *Annual Review of Fluid Mechanics*, **19**, 1987, 125–155.

[8] Raffel, M., Willert, C. and Kompenhans, J. *Particle Image Velocimetry. A Practical Guide*, Springer, 1998.

[9] Smits, A.J. and Lim. T.T. *Flow Visualization: Techniques and Examples*, Imperial College Press, 2000.

[10] Soria, J. The effects of transverse plate surface vibrations on laminar boundary layer flow and convective heat transfer, PhD Thesis *The University of Western Australia*, 1988.

[11] Soria, J. An adaptive cross-correlation digital PIV technique for unsteady flow investigations, *1st Australian Conference on Laser Diagnostics in Fluid Mechanics and Combustion*, A Masri, D. Honnery (Eds) The University of Sydney, 1996, 29–45.

[12] Soria, J. An investigation of the near wake of a circular cylinder using a video-based digital cross-correlation particle image velocimetry technique, *Experimental Thermal and Fluid Science*, **12** 1996, 221–233.

[13] Soria, J, Cater, K. and Kostas, J. High resolution multigrid cross-correlation digital PIV measurements of a turbulent starting jet using half-frame-image-shift film recording, *Optics and Laser Technology*, **31**, 1999, 3–12.

[14] Westerweel, J. Efficient detection of spurious vectors in particle image velocimetry data *Experiments in Fluids* **16**, 1994, 236–247.